

## Article

# Multi-Functional Materials Based on Cu-Doped TiO<sub>2</sub> Ceramic Fibers with Enhanced Pseudocapacitive Performances and Their Dielectric Characteristics

Petronela Pascariu \*, Mihaela Homocianu , Loredana Vacareanu and Mihai Asandulesa 

"Petru Poni" Institute of Macromolecular Chemistry, 41A Grigore Ghica Voda Alley, 700487 Iasi, Romania

\* Correspondence: dorneanu.petronela@icmpp.ro or pascariu\_petronela@yahoo.com

**Abstract:** In this work, pure TiO<sub>2</sub> and Cu (0.5, 1, 2%)-doped TiO<sub>2</sub> composites prepared by electrospinning technique followed by calcination at 900 °C, and having high pseudocapacitive and dielectric characteristics were reported. These nanocomposites were characterized by scanning electron microscopy, X-ray diffraction, and dynamic water sorption vapor measurements. The structural characterization of these nanostructures highlighted good crystallinity including only the rutile phase. The electrochemical characteristics were investigated by cyclic voltammetry and galvanostatic charge–discharge measurements, which were performed in a KOH electrolyte solution. Among the Cu-doped TiO<sub>2</sub> nanostructures that were prepared, the one containing 0.5% Cu exhibited superior electrochemical properties, including high specific gravimetric capacitance of 1183 F·g<sup>-1</sup>, specific capacitance of 664 F·g<sup>-1</sup>, energy density of 45.20 Wh·kg<sup>-1</sup>, high power density of 723.14 W·kg<sup>-1</sup>, and capacitance retention of about 94% after 100 cycles. The dielectric investigation shows good dielectric properties for all materials, where the dielectric constant and the dielectric loss decreased with the frequency increase. Thus, all the interconnected studies proved that these new materials show manifold ability and real applicative potential as pseudocapacitors and high-performance dielectrics. Future work and perspectives are anticipated for characterizing electrochemical and dielectric properties for materials including larger amounts of Cu dopant.

**Keywords:** electrospinning; titanium dioxide (TiO<sub>2</sub>) and Cu (0.5, 1, 2%)-doped TiO<sub>2</sub>; electrochemical performance; cycle life; supercapacitors



**Citation:** Pascariu, P.; Homocianu, M.; Vacareanu, L.; Asandulesa, M. Multi-Functional Materials Based on Cu-Doped TiO<sub>2</sub> Ceramic Fibers with Enhanced Pseudocapacitive Performances and Their Dielectric Characteristics. *Polymers* **2022**, *14*, 4739. <https://doi.org/10.3390/polym14214739>

Academic Editors: Maila Castellano, Andrea Doderio and Silvia Vicini

Received: 11 October 2022

Accepted: 2 November 2022

Published: 4 November 2022

**Publisher's Note:** MDPI stays neutral with regard to jurisdictional claims in published maps and institutional affiliations.



**Copyright:** © 2022 by the authors. Licensee MDPI, Basel, Switzerland. This article is an open access article distributed under the terms and conditions of the Creative Commons Attribution (CC BY) license (<https://creativecommons.org/licenses/by/4.0/>).

## 1. Introduction

Nowadays, electrochemical capacitors used as energy storage devices are attracting special attention due to their fast charge and discharge characteristics, high power density, low cost, long cycle life, and environmental friendliness [1,2]. One-dimensional (1D) nanostructures have superior properties (high aspect-ratio structure, chemical stability, large specific surface area, excellent electronic or ionic charge transfer [3]) compared to 0-dimensional and bulk materials [4,5], where the former is successfully used in supercapacitors and electrochemical energy storage applications. There are a wide variety of oxide semiconductors, including TiO<sub>2</sub>, MnO<sub>2</sub>, NiO, MoO<sub>3</sub>, Co<sub>3</sub>O<sub>4</sub>, etc. used as electrodes for supercapacitor applications [6,7]. It is known that TiO<sub>2</sub> is an excellent dielectric material with a faradaic charge storage behavior [8,9], is cost-effective, and is found in abundance, but when TiO<sub>2</sub> alone is used as a supercapacitor electrode, its behavior is relatively poor [10]. Therefore, combining TiO<sub>2</sub> with a different metal or nonmetal (Cu [11], Ni [12], Mn [13], Co [14]) can lower the bandgap energy, improve the optical response, and increase the charge carrier concentration, which all enhance the supercapacitive properties and power conversion efficiency of the new system [11,15,16]. For example, Krishnan et al. found that Ni as a dopant in TiO<sub>2</sub> nanofibers increases the conductivity and improves the specific capacitance from 40 to 179 F·g<sup>-1</sup>, for current density 1 A·g<sup>-1</sup> [17]. Another group reported improved specific capacitance after TiO<sub>2</sub> was doped with 2% Ta. They found that the

specific capacity value for 2% Ta doped TiO<sub>2</sub> nanofibers was 199 F·g<sup>-1</sup> compared to TiO<sub>2</sub>, which was 111 F·g<sup>-1</sup> for a scan rate of 5 mV/s in 1M H<sub>2</sub>SO<sub>4</sub> electrolyte. Additionally, these materials have shown excellent cycle stability (about 100% retention in specific capacity after 3000 cycles) [18].

The method of preparation, morphology, and the related structure of the TiO<sub>2</sub>/metals play an important role in the electrochemical profile/performance of these materials [19]. Therefore, 1D materials are attractive for this field due to their advantages as they have a large specific surface area, the transport of electrons occurs in one direction, and the construction of the device is easier [20]. The most important methods for obtaining these materials are electrospinning, electrodeposition [21], and anodization [22]. On the other hand, electrospinning is a relatively easy technique, versatile, and a low-cost method. Composite nanofibers with controlled diameters, adjustable compositions, high porosity, low density, and complex organic/inorganic structures with large surfaces were obtained [23]. Lal et al. fabricated a novel structure of Cu/CuO/PCNF/TiO<sub>2</sub> composites that are uniformly covered by TiO<sub>2</sub> nanoparticles and synthesized using the electrospinning method together with a hydrothermal technique, followed by air stabilization and carbonization processes to enhance the performance. These developed electrode materials showed a high specific capacitance value of 330 F·g<sup>-1</sup> at a current density of 1 A·g<sup>-1</sup> with 78.8% capacitance retention for up to 10,000 cycles and, simultaneously, a high energy density of 45.83 Wh·kg<sup>-1</sup> at a power density of 1.27 kW·kg<sup>-1</sup> [24]. Recently, Kumar et al. synthesized asymmetric Ag–Cu<sub>2</sub>O hybrid nanoparticles on graphene substrates by the hydrothermal method as an efficient electrode material for hybrid supercapacitors. They reported a specific capacitance of approx. 812 F·g<sup>-1</sup>, high energy density of 285 W·kg<sup>-1</sup>, and power density of 27.2 Wh·kg<sup>-1</sup>. The corresponding measurements were carryout at a current density of 0.5 A·g<sup>-1</sup>. Additionally, these systems showed good stability up to 2000 cycles [25].

In an attempt to enlarge the library of metal-oxide semiconductors based on TiO<sub>2</sub>, we recently reported on the design and synthesis of Cu-doped TiO<sub>2</sub> materials with novel conceptual electrochemical, pseudocapacitive, and electrical conductivity properties that were comparatively studied with regard to the most advantageous combination and synergism of the constitutive structural elements. The findings reported in this previous study prompted further investigations in order to understand how the amount of Cu dopant influences different pseudocapacitance and dielectric parameters. Therefore, pure TiO<sub>2</sub> and Cu-doped TiO<sub>2</sub> nanocomposites were prepared by electrospinning technique followed by calcination at 900 °C. The structural confirmation was monitored by scanning electron microscopy (SEM), X-ray diffraction (XRD), and dynamic water sorption vapor (DVS) measurements. To highlight the main features and applicative potential of these new materials, the electrochemical characteristics were investigated by cyclic voltammetry (CV) and galvanostatic charge–discharge (GCD) measurements. Additionally, the dielectric and conductivity properties of TiO<sub>2</sub> and Cu-TiO<sub>2</sub> nanostructures were investigated. Thus, these investigations provided the necessary tools to build a pathway for understanding the influence of Cu dopant on the smart behavior of resulting nanocomposites. In the end, all the interconnected studies proved that these new materials show manifold ability and real applicative potential as pseudocapacitors and high-performance dielectrics.

## 2. Materials and Methods

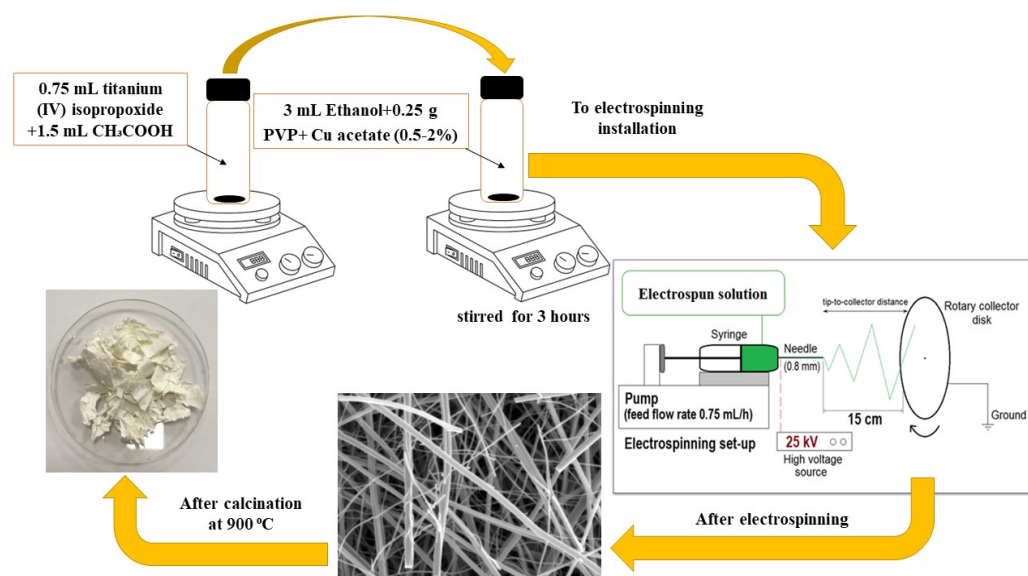
### 2.1. Materials

Nanostructures of pure TiO<sub>2</sub> and Cu-doped TiO<sub>2</sub> were obtained by the electrospinning method using identical preparation parameters, but calcined at 900 °C according to our previous work [26]. Titanium (IV) isopropoxide (TTIP) (~97%, CAS: 546–68–9), copper acetate [Cu(CH<sub>3</sub>COO)<sub>2</sub>·H<sub>2</sub>O] (≥98%, CAS: 6046–91–1), glacial acetic acid (CH<sub>3</sub>COOH) (99–100%, CAS: 64–19–7), ethanol (96%, CAS: 64–17–5), polyvinylpyrrolidone (PVP) (Mw = 1.300.000, CAS: 9003–39–8), polyvinylidene fluoride (PVDF) (Mw = 275.000 g/mol, CAS: 24937–79–9), potassium hydroxide (KOH) (≥85%, CAS: 1310–58–3), N,N-dimethylformamide (DMF) (99.8%, CAS: 68–12–2); all the precursors used in obtaining these materials were purchased

from Sigma-Aldrich Co. (Taufkirchen, Germany) and used without further purification. Conductive carbon black (size = 20 nm, CAS: 1333-86-4) was purchased from PowderNano.

## 2.2. $\text{TiO}_2$ and Cu-Doped $\text{TiO}_2$ Composite Preparations

The electrospinning method was used to prepare pure  $\text{TiO}_2$  and Cu-doped  $\text{TiO}_2$  nanostructures according to the procedure described in a previous paper, but calcined in air at  $900\text{ }^\circ\text{C}$ , with a  $15\text{ }^\circ\text{C}/\text{min}$  heating rate [26]. Briefly, pure and doped nanofibers were prepared using electrospun solutions, composed by mixing two solutions, namely: 0.75 mL of TTIP in 1.5 mL acetic acid (solution 1) and 0.25 g PVP in 3 mL ethanol (solution 2). This mixed solution was used to obtain the pure  $\text{TiO}_2$  blank sample (T2). Cu-doped  $\text{TiO}_2$  composites were obtained by adding to solution 2 various amounts (0.5, 1, and 2% by weight) of Cu acetate. These two solutions were mixed and the resulting homogeneous solution was transferred to an electrospinning syringe. All materials were prepared using a homemade electrospinning installation according to our previous studies [27]. Finally, the obtained nanofibers were calcined at  $900\text{ }^\circ\text{C}$  for 4 h. The samples prepared according to steps from Scheme 1 were tagged as T2 for pure  $\text{TiO}_2$ , CT2 for 0.5% Cu- $\text{TiO}_2$ , CT3 for 1% Cu- $\text{TiO}_2$ , and CT4 for 2% Cu- $\text{TiO}_2$ .



**Scheme 1.** Preparation of the pure and Cu-doped  $\text{TiO}_2$  nanostructures.

## 2.3. Characterization of the Prepared Materials

A Rigaku SmartLab-9kW (Rigaku Corporation, Tokyo, Japan) diffractometer was used to record the XRD patterns of samples and to examine their crystalline structure. The morphological analysis of the Cu-doped  $\text{TiO}_2$  materials was investigated using a Verios G4 UC Scanning Electron Microscope (Thermo Fisher Scientific, Brno, Czech Republic) equipped with an energy dispersive spectrometer (EDS, EDAX Octane Elite). A fully automated gravimetric analyzer, IGAcorp, supplied by Hiden Analytical, Warrington (UK), with an ultrasensitive microbalance, was used to measure the dynamic water vapor sorption capacity of the samples as the weight changes with variation in humidity at a constant temperature. Each sample was dried in flowing nitrogen ( $250\text{ mL}/\text{min}$ ) until the weight of the sample was in equilibrium at  $\text{RH} < 1\%$ . Experiments were carried out at  $25\text{ }^\circ\text{C}$  in the relative humidity (RH) range of 0–90%, with 10% humidity steps, each having a pre-established equilibrium time between 40 and 60 min (minimum time and time out, respectively). The Brunauer–Emmett–Teller (BET) method was used to calculate the specific surface areas of the samples [28]. Broadband dielectric spectroscopy measurements were recorded with a Novocontrol Concept 40 Broadband Dielectric Spectrometer device. The dielectric spectra were recorded isothermally in broad frequency (between 1 Hz to 1 MHz) and temperature (between  $-150$  and  $200\text{ }^\circ\text{C}$ ) ranges. Alternating electrical field oscillations

were furnished by an Alpha-A frequency analyzer, and the temperature was controlled to better than 0.1 °C with a Quatro Cryosystem device. The powder samples were obtained as pressed circular pellets with 13 mm diameter and ca. 0.25 mm thick. After preparation, the samples were sandwiched between two cylindrical gold-plated electrodes (furnished by Novocontrol, Montabaur, Germany) and then mounted between the electrodes of the BDS active sample cell.

#### 2.4. Electrochemical Characterization

The electrochemical measurements were performed using a Voltalab PST050 electrochemical workstation with a three-electrode system using a 1 M KOH electrolyte solution at room temperature. A platinum wire was used as the auxiliary electrode, Ag/AgCl as the reference electrode, pure and Cu-doped TiO<sub>2</sub> on nickel foam as the working electrode. This electrode was prepared according to the following protocol: 80 wt% of TiO<sub>2</sub> and Cu (0.5, 1, 2%)-doped TiO<sub>2</sub> nanostructures, 10 wt% of carbon black, and 10% PVDF dissolved in DMF. These mixtures were dropped on Ni foam supports (previously cleaned with ethanol in an ultrasonic bath) and then dried for 12 h at 60 °C [29]. In our experiments, the amounts of pure TiO<sub>2</sub> and Cu-doped TiO<sub>2</sub> on the Ni foam electrode were approximately 5.98, 4.84, 6.48, and 6.25 mg, respectively. The specific capacitance of pure and Cu-doped TiO<sub>2</sub> composites was studied by galvanostatic charge–discharge measurements recorded for a potential between 0 and 0.7 V at a current of 10 mA.

### 3. Results

#### 3.1. XRD Analysis

The crystalline structure of the prepared materials was examined by XRD measurements. XRD data were collected in the 2 $\theta$  range from 20 to 80° with a scanning rate of 1°/min and a step size of 0.01°. Figure 1 shows the diffraction profiles of pure TiO<sub>2</sub> and Cu (0.5, 1, 2%) doped TiO<sub>2</sub> calcined at 900 °C. These nanostructures showed good crystallinity containing only the rutile phase. It is known that rutile is the predominant phase during the calcination of TiO<sub>2</sub> materials at 900 °C [30]. All studied composites highlighted diffraction peaks at 27.47°, 36.03°, 39.23°, 41.28°, 44.09°, 54.35°, 56.66°, 62.79°, 64.07°, 69.07°, and 69.80°, corresponding to the rutile phase of TiO<sub>2</sub> and associated with the crystallographic planes (110), (101), (200), (111), (210), (211), (220), (002), (310), (301), and (112), respectively. We note that no additional peaks were identified, which means that the Cu ions were fully integrated into the rutile structure of TiO<sub>2</sub> [14]. Additionally, composites prepared at different Cu concentrations have slight leftward shifts in the peak position compared to pure TiO<sub>2</sub> (inset of Figure 1). Moreover, we found that the intensity of the diffraction peaks decreases with increasing Cu concentration. The most important structural parameters, including the average crystallite size (D), unit cell parameters (a, c), Ti-O-Ti bond length (L), unit cell volume values (V), and the micro-deformation ( $\epsilon$ ) were determined using different relationships defined in our previous studies [31,32], while the obtained values are listed in Table 1. The average D values decreased significantly for Cu-doped TiO<sub>2</sub> from about 40 to 20 nm, due to the inhibition of crystallite growth after the inclusion of copper ions into the crystal structure of TiO<sub>2</sub> [14,33]. Moreover, the cell parameter increases after Cu doping in the lattice together with an increase in volume, while the cell parameter c decreased slightly, demonstrating that Cu was successfully incorporated into the lattice. The full width at half-maximum (FWHM) values increased from 0.17 to 0.42 with increasing copper content from 0.5 to 2% in the composites [34].

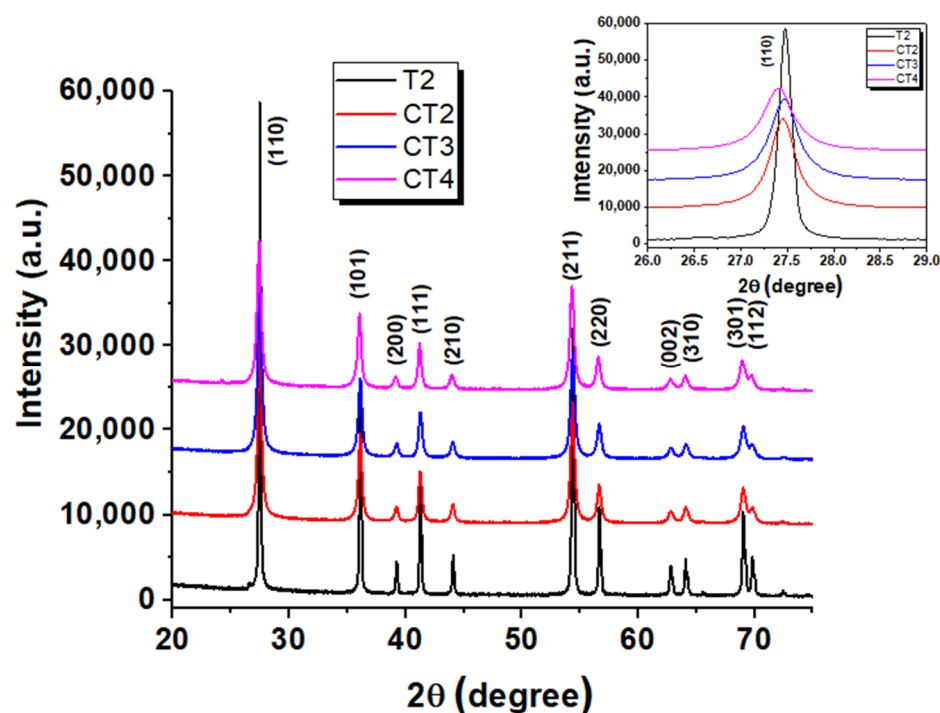


**Figure 1.** XRD diffraction profiles of pure TiO<sub>2</sub> (T2) and Cu (0.5, 1, 2%)-doped TiO<sub>2</sub> (CT2-CT4) composites.

**Table 1.** The values of the lattice parameters (crystallographic planes ( $d_{hkl}$ ), the average crystallite size (D, nm), unit cell parameters ( $a$ ,  $c$ , Å), Ti-O-Ti bond length (L, nm), and the micro-deformation ( $\epsilon$ , %) and volume (V, Å<sup>3</sup>) of pure TiO<sub>2</sub> and Cu-doped TiO<sub>2</sub> nanostructures.

Samples	$2\theta$ (°)	( $hkl$ )	$d_{hkl}$ (Å)	FWHM (°)	D (nm)	$a$ (Å)	$c$ (Å)	$\epsilon$ (%)	L (nm)	V (Å <sup>3</sup> )
T2	27.47	(110)	3.244	0.17	48.05	4.588	-	0.174	4.035	53.90
	36.11	(101)	2.485	0.21	39.67	-	2.957	0.203	-	-
CT2	27.45	(110)	3.247	0.34	23.98	4.592	-	0.348	4.041	53.99
	36.10	(101)	2.486	0.35	23.80	-	2.957	0.268	-	-
CT3	27.47	(110)	3.244	0.42	19.41	4.589	-	0.429	4.037	53.91
	36.11	(101)	2.485	0.38	21.92	-	2.956	0.291	-	-
CT4	27.41	(110)	3.251	0.42	19.41	4.598	-	0.431	4.050	54.25
	36.03	(101)	2.491	0.40	20.82	-	2.963	0.308	-	-

### 3.2. Morphological Characterization

The surface morphology of pure TiO<sub>2</sub> and the Cu-doped TiO<sub>2</sub> nanostructures were examined by SEM imaging, as shown in Figure 2. The nanofibers were round, fully interconnected, and exhibited a uniform diameter distribution (Figure 2a). These images depicted the presence of Cu dopant that was negligibly agglomerated and distributed along the axial direction of the nanofibers (Figure 2b,d). The presence of Cu dopant was evidenced by the EDS spectra presented in Figure S1 in the Supplementary Materials. The presence of platinum in the EDS analysis results from the sample preparation for SEM/EDS measurements. The atomic percentage of Cu recorded in the material varied between 0.31% and 0.57%, depending on the amount of precursor solutions it contained in the initial composition. Moreover, no other impurities were found. As can be seen from the EDS mapping images shown in Figure S2, these materials have good homogeneity of elements. According to the histograms reported in Figure S3, the average size of the fiber diameters

varies between 150 and 200 nm. These histograms were obtained by measuring 100 fiber diameters for each material and prepared using Image-J software (Java 1.8.0\_345 (64-bit)).

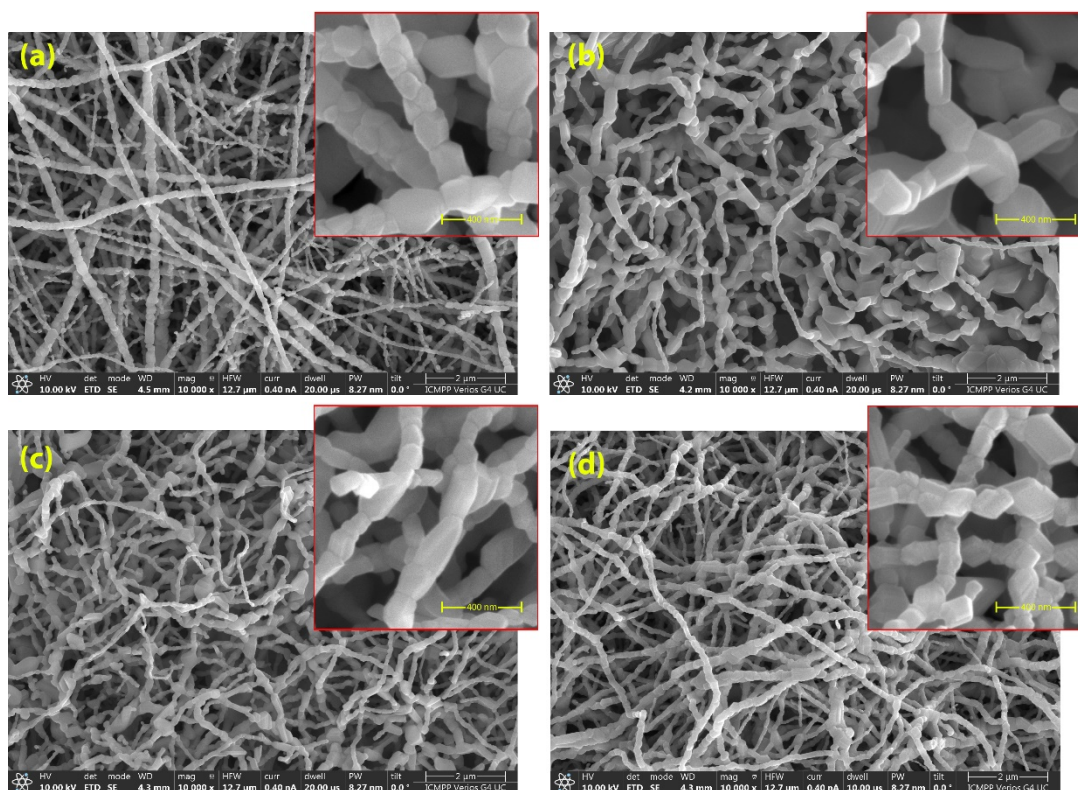


**Figure 2.** SEM images for pure TiO<sub>2</sub> (a) and 0.5% (b), 1% (c), and 2% (d) Cu-doped TiO<sub>2</sub> composites.

### 3.3. Sorption and Desorption Isotherms

It is known that materials with a large specific surface area can provide several active surface places and facilitate the transport of ions, improving the electrochemical performance of the materials [14]. The adsorption and desorption isotherms of pure TiO<sub>2</sub> and Cu-doped TiO<sub>2</sub> nanostructures are shown in Figure 3. From these isotherms, it can be seen that water desorption is faster than water sorption for all samples, which highlights their hysteresis behavior. The water adsorption–desorption isotherms (Figure 3) show the dependence between the equilibrium water content of the composites and relative humidity (RH), and are used to estimate the sorption capacity, average pore size, and specific surface area of the prepared materials (Table 2). Below 30% RH, the mass changes were negligible compared to the initial weight and showed no significant modifications when the Cu dopant content was varied (Figure 3). At more than 30% RH, the mass changes increased exponentially with RH values. At 80% RH, the mass change was higher for the 0.5% Cu-TiO<sub>2</sub> composite. The sorption capacities of the prepared composites were correlated with their hysteresis behavior and were found to have the highest values for the 0.5% Cu-TiO<sub>2</sub> composite (12.30% d.b.). From Table 2, it can be seen that the addition of copper dopant increased the pore size (from 1.7 nm for pure TiO<sub>2</sub> to 4.31 nm for 0.5% Cu-TiO<sub>2</sub>) and their sorption capacity values. The BET surface area (Table 2) for pure TiO<sub>2</sub> is 112 m<sup>2</sup>/g, but with increasing Cu-doping concentration, a decrease in surface area values was observed due to a larger ionic radius of Cu ions (0.72 Å) than that of Ti ions (0.68 Å). Ganesh et al. also reported that upon increasing the Cu-doping concentration in TiO<sub>2</sub> thin film, BET surface area values decreased [35]. The lowest surface area value (57.2 m<sup>2</sup>/g) is for 0.5% Cu-TiO<sub>2</sub> having the largest average pore size (4.31 nm, Table 2).

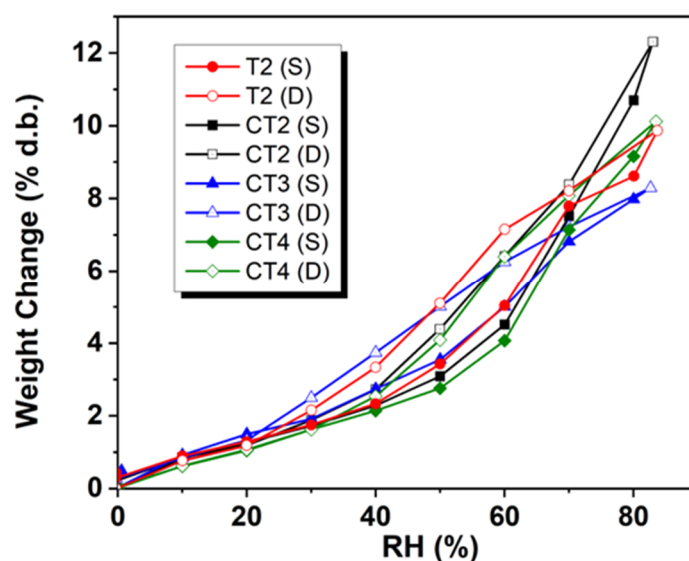


Figure 3. Adsorption (S) and desorption (D) isotherms for pure TiO<sub>2</sub> and Cu-doped TiO<sub>2</sub> composites.

Table 2. Dynamic water sorption vapor data for the tested materials.

Sample	Sorption Capacity, % d.b.	Average Pore Size, nm	BET Data	
			Area, m <sup>2</sup> /g	Monolayer, g/g
T2	9.86	1.77	112	0.031
CT2	12.30	4.31	57.2	0.0163
CT3	8.30	2.41	69	0.0196
CT4	10.10	3.19	63.5	0.0181

### 3.4. Electrochemical Characterization

The electrochemical performance of Cu-doped TiO<sub>2</sub> nanostructures compared to pure TiO<sub>2</sub> was evaluated by CV, GCD, and stability measurements. Figure 4 shows the CV curves, which demonstrate the pseudocapacitive behavior given by the redox reaction pairs (with good redox symmetry) [36] and good stability recorded for all samples. According to these curves, the capacitance characteristics are dominated by faradaic reactions and are different from those of double-layer electric capacitors [37]. The area of the CV curves increases significantly from pure TiO<sub>2</sub> electrodes to Cu-doped TiO<sub>2</sub> (Figure 4), suggesting better capacitive behavior of the composite materials compared to pure TiO<sub>2</sub>. Additionally, as the scan rate increased, a similar shape and an increase in anodic peak currents (during direct and reversed sweep) were observed (Figure 4), demonstrating reversibility [38] and good capacitive behavior. The pseudocapacitance behavior may be due to the interconversion between oxidation states of Cu(I) and Cu(II) [25] representing anodic and cathodic peaks (Figure 4). From the CV curves, it can be observed that the magnitude (current densities) of the oxidation (0.37 V) and reduction (0.47 V) peaks are higher for 0.5% Cu-TiO<sub>2</sub> compared to other samples (CT3), indicating higher capacitance for this sample.

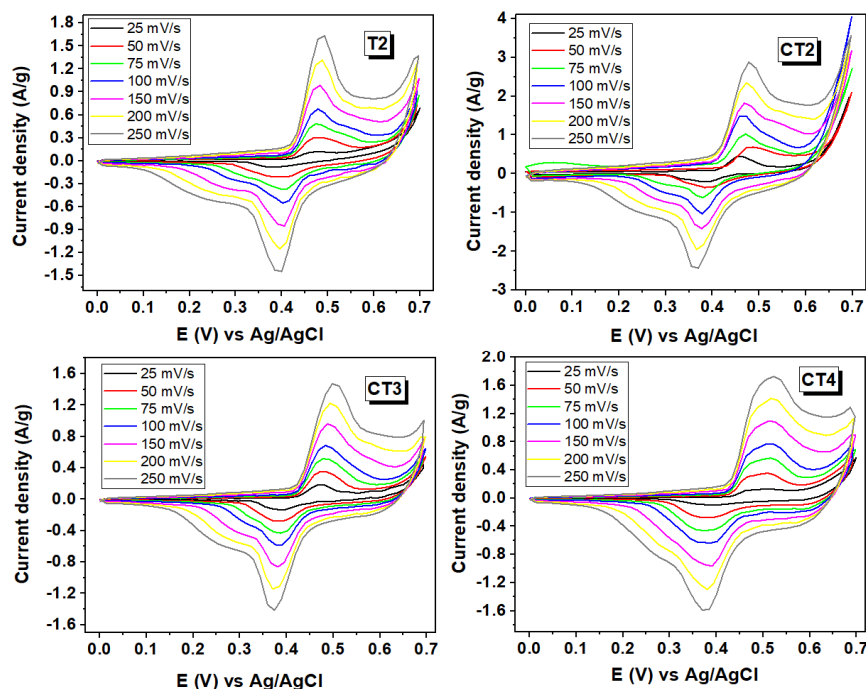


Figure 4. Cyclic voltammetry curves of pure TiO<sub>2</sub> (T2) and 0.5% Cu (CT2), 1% Cu (CT3), 2% Cu (CT4) doped TiO<sub>2</sub> nanostructures, at different scan rates.

Figure 5 shows the cyclic voltammetry comparison curves of pure TiO<sub>2</sub> and Cu (0.5, 1, 2%)-doped TiO<sub>2</sub> composites recorded at scanning rates of 25, 50, 150, and 250 mV/s. All these curves exhibited oxidation and reduction peaks positioned at the potentials of 0.46 and 0.52 V, whose intensities increased with increasing scanning speed values. The area under the CV curves for the 2% Cu-TiO<sub>2</sub> composite at 250 mV/s was larger than the area under the CV curves for TiO<sub>2</sub>, 0.5% Cu-TiO<sub>2</sub>, and 1% Cu-TiO<sub>2</sub> (Figure 5), indicating an enhanced capacitance for this composite.

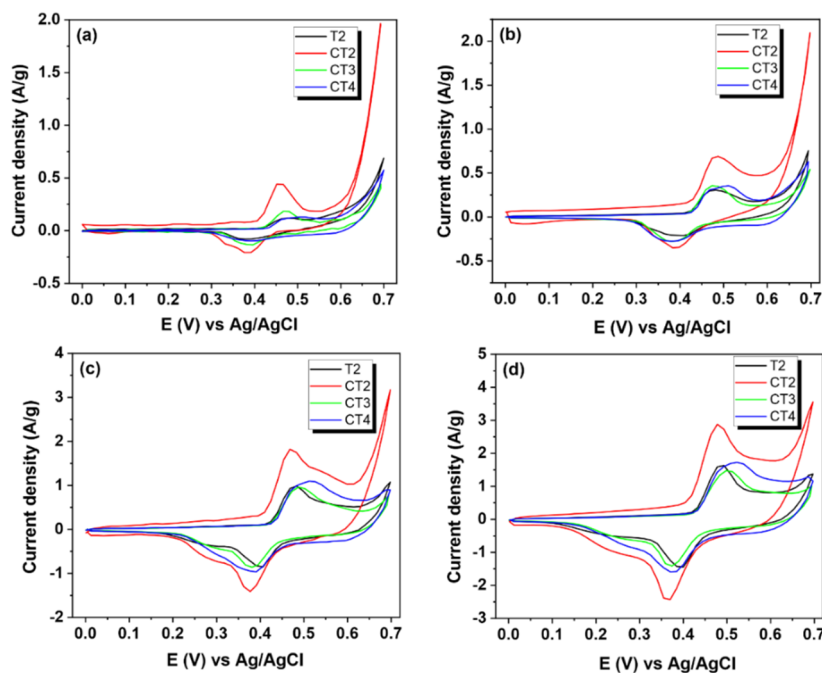
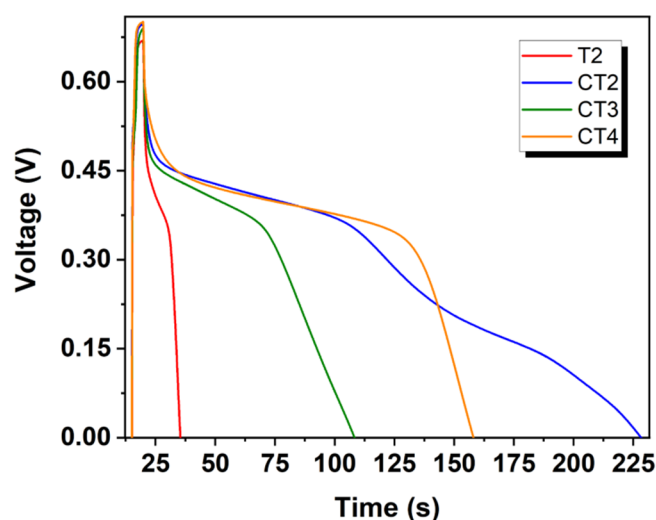


Figure 5. Cyclic voltammetry curves for TiO<sub>2</sub> (T2) and Cu (0.5%, 1%, 2%)-doped TiO<sub>2</sub> (CT2-CT4) recorded at 25 mV/s (a); 50 mV/s (b); 150 mV/s (c); and 250 mV/s (d) scan rates.

To study in detail the electrochemical properties of pure TiO<sub>2</sub> and Cu-doped TiO<sub>2</sub> composites, we employed the investigation of the GCD curves. Figure 6 shows the GCD curves of pure TiO<sub>2</sub> and Cu-TiO<sub>2</sub> composites that display asymmetry, suggesting that the materials undergo redox reactions according to cyclic voltammetry curves (Figure 5). After this plateau, it can be seen that the voltage decreases sharply due to the internal resistance of the material in the part of the discharge curve [39]. Moreover, the GCD curves of the composites exhibited asymmetry and good reversibility, indicating faradaic pseudocapacitance behavior [40].



**Figure 6.** Galvanostatic charge–discharge curves of pure TiO<sub>2</sub> (T2) and Cu-TiO<sub>2</sub> (CT2–CT4) composites.

Based on the galvanostatic charge–discharge curves, the specific capacitance (C<sub>SP</sub>, F·g<sup>−1</sup>), [18] the energy density (*E*, Wh·kg<sup>−1</sup>) [41], and power density (*P*, W·kg<sup>−1</sup>) [42] were calculated by applying the following relationships:

$$C_{SP} = \frac{\int IV}{2mV} \text{ (gravimetric)} \quad (1)$$

$$C_{SP} = \frac{I \times t}{V \times m} \quad (2)$$

$$E = \frac{C_{SP} \times \Delta V^2}{7.2} \quad (3)$$

$$P = \frac{E \times 3600}{\Delta t} \quad (4)$$

where *C<sub>SP</sub>*, *I*, *Δt*, *ΔV*, and *m* are the specific capacitance, the charge–discharge current (A), the discharging time (s), the applied potential window (V), and the active mass of the electrode (g), respectively.

From galvanostatic charge–discharge measurements, it was found that the 0.5% Cu-doped TiO<sub>2</sub> (CT2) nanostructure showed a longer charge–discharge time than the other doped materials (CT3, CT4), demonstrating the highest specific capacitance. Several factors can affect the specific capacitance of the electrode materials, including specific surface area, shape, nanostructure size, and conductivity [14]. Figure 7 shows the dependence of specific gravimetric capacitance on scan rates. According to Figure 7 and Table 3, we found that the maximum capacitance value of 1183.89 F·g<sup>−1</sup> (at 0.15 V/s) corresponds to sample CT2 (with 0.5% Cu). Pure TiO<sub>2</sub> had a specific capacitance value of 526 F·g<sup>−1</sup> (at 0.15 V/s), which is higher than previously reported for some other TiO<sub>2</sub>-based electrodes [29,43,44]. For example, Pant et al. [29] reported that TiO<sub>2</sub> carbon nanofibers can be successfully used as electrodes for supercapacitors due to their outstanding specific properties, including

specific capacity ( $106.57 \text{ F}\cdot\text{g}^{-1}$ ) and 84% capacity retention after 2000 cycles. Likewise, He et al. prepared electrode material based on  $\text{TiO}_2$  nanofiber using an electrospinning technique and then treated them in KOH. The specific capacity found for this material improved dramatically from  $0.04 \text{ F}\cdot\text{g}^{-1}$  (for untreated  $\text{TiO}_2$ ) to  $65.84 \text{ F}\cdot\text{g}^{-1}$  at  $1 \text{ mV/s}$  [43].

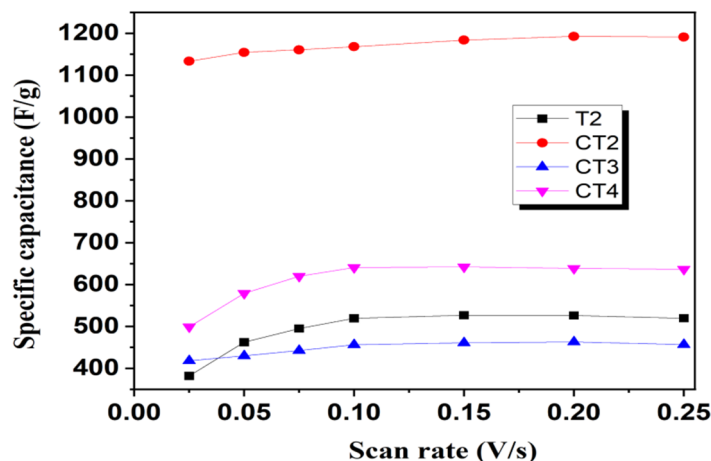


**Figure 7.** The evolution of specific gravimetric capacitance at the different scan rates for pure  $\text{TiO}_2$  and Cu-doped  $\text{TiO}_2$  composites.

**Table 3.** Data obtained from cyclic voltammetry and galvanostatic charge–discharge curves for pure  $\text{TiO}_2$  and Cu- $\text{TiO}_2$  electrodes.

Electroactive Materials	Specific Gravimetric Capacitance ( $\text{F}\cdot\text{g}^{-1}$ )	Specific Capacitance ( $\text{F}\cdot\text{g}^{-1}$ )	Energy Density ( $\text{Wh}\cdot\text{kg}^{-1}$ )	Power Density ( $\text{W}\cdot\text{kg}^{-1}$ )
T2	526	84	5.69	585.28
CT2	1183.89	664	45.20	723.14
CT3	456	235	16.05	540.12
CT4	640	361	24.56	559.55

The specific capacitance, energy density, and power density values for all evaluated materials using Equations (1)–(4) are listed in Table 3. From these results, it is clear that Cu-doped  $\text{TiO}_2$  shows better electrochemical performance compared to the pure  $\text{TiO}_2$  nanoparticles, suggesting that copper contributes to the improvement of the electronic conductivity of  $\text{TiO}_2$ . Therefore, the highest values for energy density ( $45.20 \text{ Wh}\cdot\text{kg}^{-1}$ ) and power density ( $723.14 \text{ W}\cdot\text{kg}^{-1}$ ) were found for 0.5% Cu-doped  $\text{TiO}_2$  composite.

The life cycle stability is a key characteristic of supercapacitors, so for the pure  $\text{TiO}_2$  and Cu- $\text{TiO}_2$  electrode materials, this parameter was evaluated by measuring the consecutive charge–discharge curves (Figure 8) for 100 cycles. From this figure, it is clear that the coulombic efficiency of Cu-doped materials ( $\sim 94\%$ ) increased compared to that of pure  $\text{TiO}_2$  (88%), suggesting good stability at 100 cycles. Moreover, the results obtained in this work indicated that the electrochemical performance of Cu-doped  $\text{TiO}_2$  is superior to pure  $\text{TiO}_2$  and is comparable to other related metal-doped  $\text{TiO}_2$  systems found in the literature (Table 4).

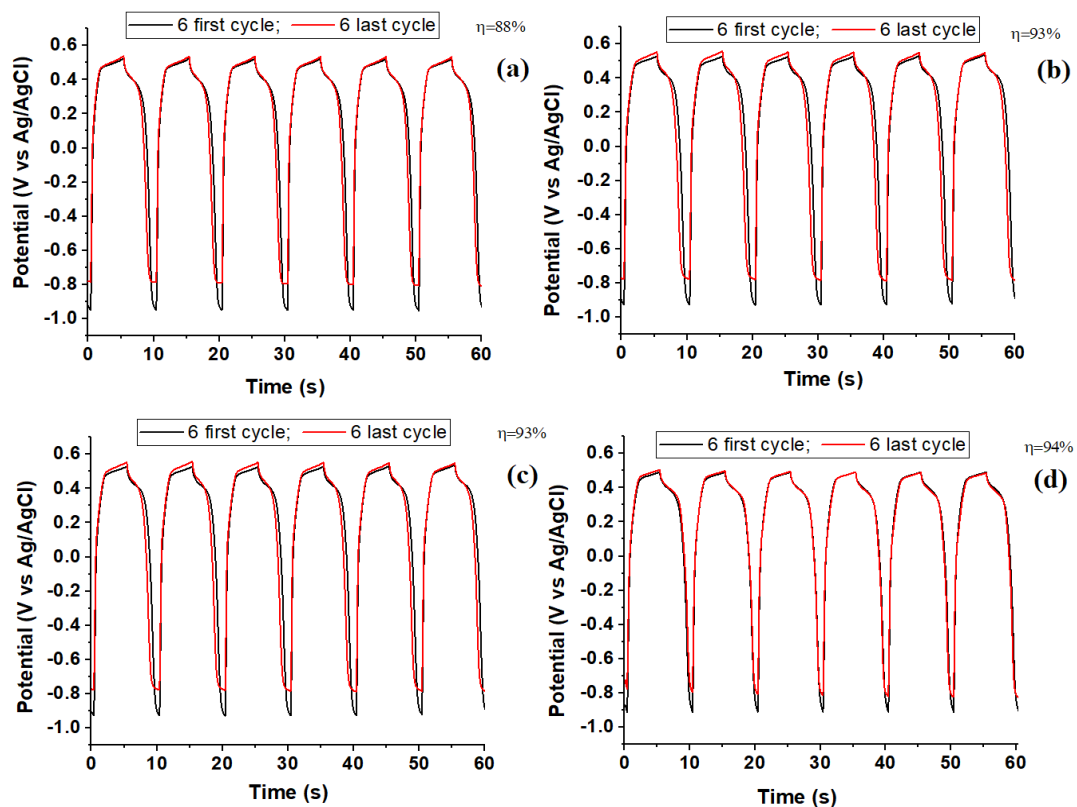


**Figure 8.** First six cycles and last five cycles of charge–discharge curves for (a)  $\text{TiO}_2$ , (b) 0.5% Cu- $\text{TiO}_2$ , (c) 1% Cu- $\text{TiO}_2$ , and (d) 2% Cu- $\text{TiO}_2$  composites.

**Table 4.** A comparison of the electrochemical properties of Cu-doped  $\text{TiO}_2$  composites with the properties of other metal-doped  $\text{TiO}_2$  systems reported in the literature.

Material	Preparation Method	Electrolyte	$C_{SP}$ ( $\text{F}\cdot\text{g}^{-1}$ )	Specific Energy ( $\text{Wh}\cdot\text{Kg}^{-1}$ )	Specific Power ( $\text{W}\cdot\text{Kg}^{-1}$ )	CS Retention (%) / Cycle Number	Ref.
Nb-doped $\text{TiO}_2$		3 M KOH	52	770	16.3	100/5000	[45]
Ta-doped $\text{TiO}_2$	electrospinning	1M $\text{H}_2\text{SO}_4$	199 at 5 mV/s	11.25	100.49	100/5000 at a current density of $1 \text{ A g}^{-1}$	[18]
Co-doped $\text{TiO}_2$	solvothermal method	3 M KOH	352 at a current density of 0.5 A/g	-	-	97/3000 at a current density of $0.5 \text{ A g}^{-1}$	[14]
Ni-doped $\text{TiO}_2$	electrospinning	3 M KOH	200 at 2 mV/s	-	-	100/5000	[17]
0.5%Cu-doped $\text{TiO}_2$	electrospinning	1 M KOH	1183.89 at 0.15 V/s	45.20	723.14	94/100	this work

### 3.5. Dielectric Spectroscopy Measurements

To obtain better insights regarding the full potential of these materials in supercapacitors, dielectric spectroscopy measurements were employed. Therefore, Figure 9a shows the behavior of the dielectric constant with the applied field frequency for the T2 sample toward the increasing temperature from  $-150$  to  $200$  °C. At low temperatures,  $\epsilon'$  is of low magnitude in the entire frequency range (e.g., at  $-100$  °C and 1 kHz,  $\epsilon' = 9.1$ ), suggesting a reduced dipolar activity. As temperature increases, the magnitude of  $\epsilon'$  is enhanced, due to the accumulation of thermal energy by the polarizable units. Moreover, at temperatures higher than  $0$  °C,  $\epsilon'$  shows a pronounced decrease, especially at low frequencies.

According to the literature, this behavior of  $\epsilon'$  is produced by the accumulation of charge carriers at the interface between the sample surfaces and the electrodes used to perform the dielectric measurements [46,47]. Undoubtedly, the electrode polarization process of the blocked charges affects the dipolar-type signal. With further increase in frequency, however, the effect of space charge polarization is diminished, revealing a moderate decrease in  $\epsilon'$ . Therefore, two different processes are distinguished: (i) the electrode polarization effect manifested at low frequencies and (ii) the dipolar activity of the sample at high frequencies. Following the  $\epsilon'(f)$  dependences of all samples (Figure 9b), no clear effect of the copper doping on the dielectric constant was observed.

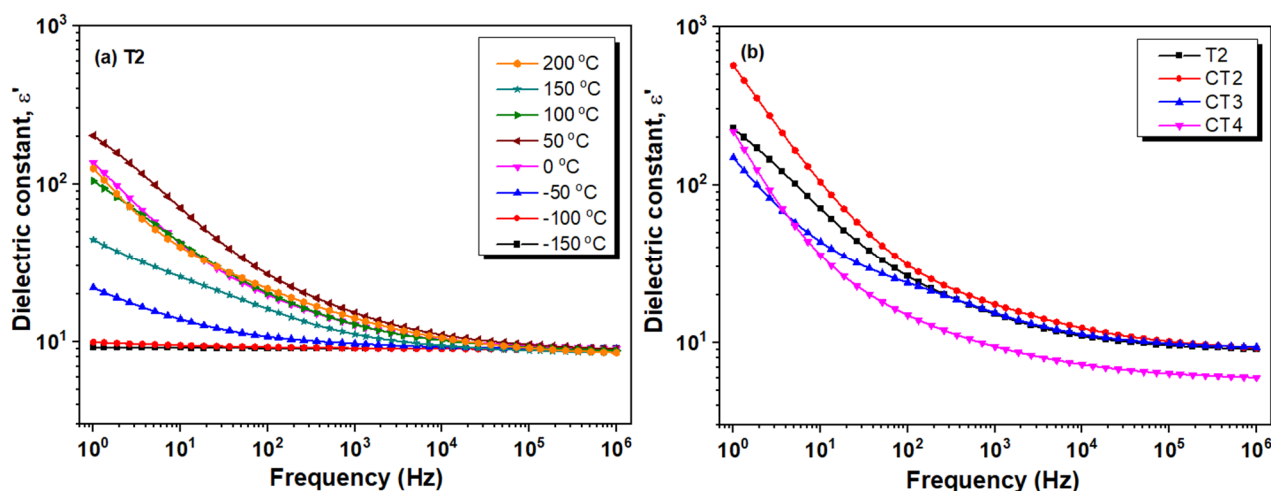


**Figure 9.** The evolution of dielectric constant as a function of frequency: (a) exemplarily for T2 at various temperatures and (b) comparatively for all examined samples at room temperature.

The isothermal plots of dielectric loss  $\epsilon''$  as a function of frequency at different temperatures are retrieved in Figure 10a for the CT2 sample. The magnitude of  $\epsilon''$  is regularly enhanced with increasing temperature in the entire frequency range, suggesting that the polarizable units are closely connected to the temperature changes. On the other hand,  $\epsilon''$  decreases gradually toward increasing frequency and presents a pronounced decrease in magnitude, in particular at low frequencies and high temperatures, in a similar way to the frequency behavior of the dielectric constant parameter. The linear decrease in  $\epsilon''$  at low frequencies suggests the existence of free charges in the material lattice [48,49]. As observed in Figure 10b,  $\epsilon''$  of copper-doped TiO<sub>2</sub> samples follow similar tendencies, with a linear decrease at low frequencies and a monotonous decrease at higher frequencies. For the T2 sample, the linear decrease at low frequencies is missing, suggesting the absence of the free charge carriers.

The behavior of the measured conductivity ( $\sigma = 2\pi\epsilon_0 f\epsilon''$ , where  $\epsilon_0$  is the vacuum permittivity and  $f$  is the frequency of the applied field) and the phase angle ( $\theta = \tan^{-1}(Z_{\text{im}}/Z_{\text{re}})$ , where  $Z_{\text{im}}$  and  $Z_{\text{re}}$  are the imaginary and the real components of the impedance) with the frequency at various temperatures are represented in a common diagram in Figure 11a for CT3 sample. At low temperatures,  $\sigma$  regularly increases toward increasing frequency and the corresponding values of  $\theta$  are detected between  $0 < \theta(f) \leq -90^\circ$ . This capacitive behavior is generally attributed to the dipolar-type relaxation processes of the material. On the other hand, at low frequencies and high temperatures, a change in the slope of the measured conductivity, correlated with the enhancement of the phase angle values close to  $0^\circ$  is observed. This behavior is of resistive type and may be assigned to the presence of mobile charge carriers in the material backbone [50]. The comparative  $\sigma(f)$ , as well as  $\theta(f)$  profiles of all examined samples retrieved in Figure 11b, show that the resistive behavior of measured conductivity is detected only for the prepared copper-doped TiO<sub>2</sub> samples. This may suggest that copper doping acts as a source of free charge carriers.

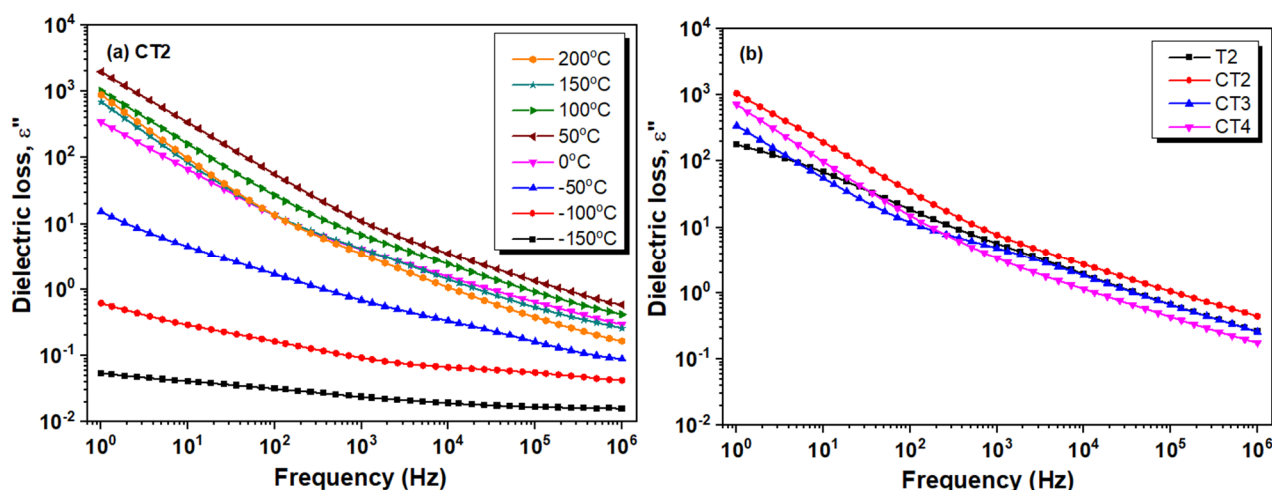


**Figure 10.** The evolution of dielectric loss as a function of frequency: (a) exemplarily for CT2 at various temperatures and (b) comparatively for all examined samples at room temperature.

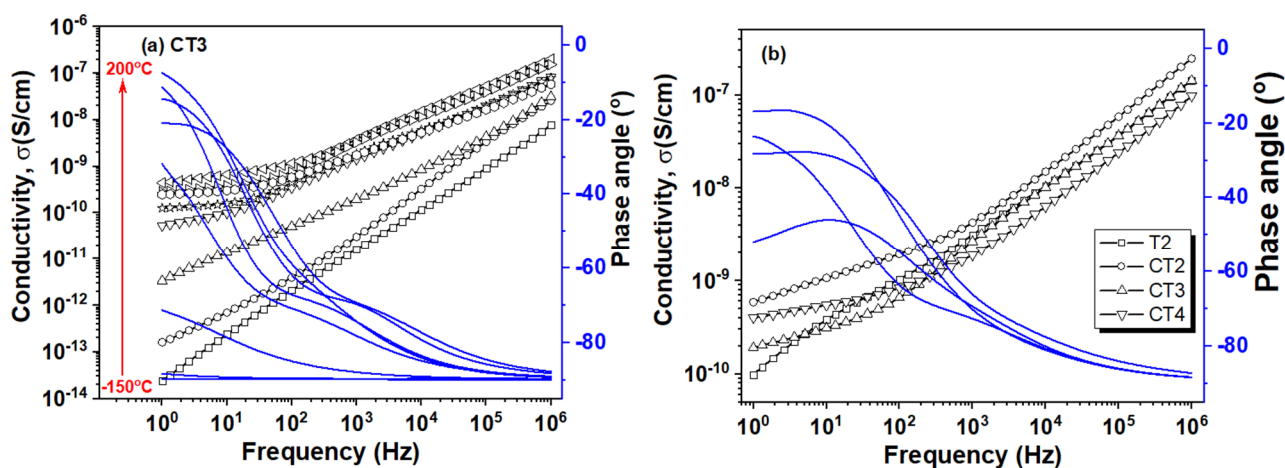


**Figure 11.** The evolution of conductivity as a function of frequency: (a) exemplarily for CT3 at various temperatures and (b) comparatively for all examined samples at room temperature.

In Figure 12a, the behavior of conductivity as a function of temperature for various frequencies is represented for the CT4 sample, as a representative example. The magnitude of  $\sigma$  increases gradually with the frequency increase. The conductivity values were further selected at a frequency of 1 Hz and were plotted as a function of temperature in Figure 12b for neat T2 and copper-doped TiO<sub>2</sub> samples. All examined samples reveal similar temperature behavior. At low temperatures, between  $-150$  °C and around  $0$  °C, all examined samples reveal a linear increase in conductivity with a similar slope and comparable values of  $\sigma$ . At temperatures higher than  $0$  °C, an inflection point is detected. It is worth mentioning that the maximum of inflection point is remarkably shifted in copper-doped TiO<sub>2</sub> samples to higher temperatures, while the maximum inflection point for T2 sample is detected around  $35$  °C,  $55$  °C for CT2,  $65$  °C for CT3, and  $48$  °C for CT4. Moreover, in the temperature region of the inflection point, the numerical values of conductivity are higher for copper-doped TiO<sub>2</sub> samples than for neat T2 samples (see Table 5 with  $\sigma$  values retrieved at room temperature).

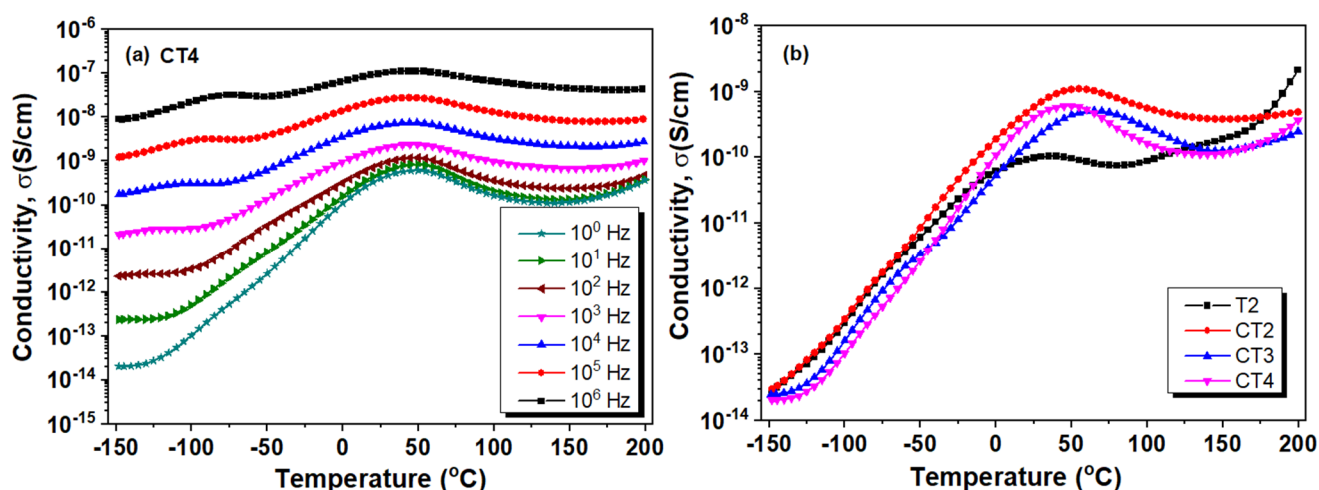


**Figure 12.** The evolution of conductivity as a function of temperature: (a) exemplarily for CT4 at various frequencies and (b) comparatively for all examined samples at room temperature.

**Table 5.** Numerical values of dielectric constant, dielectric loss and conductivity were retrieved at room temperature for all examined samples.

Sample	$\epsilon'$ (1 kHz)	$\epsilon''$ (1 kHz)	$\sigma$ (S/cm) (1 Hz)
T2	15.1	5.7	$1 \times 10^{-10}$
CT2	17.5	7.7	$6 \times 10^{-10}$
CT3	15.4	4.8	$2 \times 10^{-10}$
CT4	9.4	3.4	$4 \times 10^{-10}$

#### 4. Conclusions

The pure  $\text{TiO}_2$  and Cu- $\text{TiO}_2$  composites were prepared by electrospinning followed by carbonization at 900 °C. The obtained materials showed good crystallinity with the presence of only the rutile phase. Furthermore, the average crystallite size decreased significantly for Cu-doped  $\text{TiO}_2$  from about 40 to 20 nm. The (0.5, 1, 2%) Cu-doped  $\text{TiO}_2$  composites exhibited a higher specific capacitance, better rate capability, and cycling stability compared to pure  $\text{TiO}_2$ , although the particle size and pore size were larger and surface area was lower. It was found that the 0.5% Cu-doped  $\text{TiO}_2$  (CT2) nanostructure showed a longer charge–discharge time (227 s) than other doped materials, demonstrating the highest specific capacitance. It was found that 0.5% Cu- $\text{TiO}_2$  is the optimal dopant concentration in terms of electrochemical and capacitive performances. The maximum capacitance value obtained for this material was  $1183.89 \text{ F}\cdot\text{g}^{-1}$  (at 0.15 V/s). After 100 charge–discharge cycles, the capacitance retention of about 94% for Cu-doped  $\text{TiO}_2$  shows good cycling stability. The dielectric constant, the dielectric loss, and the dc conductivity of materials in the frequency range 10 Hz–1 MHz were measured at different temperatures. With increasing frequency and temperature, the electric conductivity increased. Therefore, regarding its use in pseudocapacitor applications, electrospun Cu-doped  $\text{TiO}_2$  nanostructures exhibit superior electrochemical properties compared to pure  $\text{TiO}_2$ . To determine to what extent and how this can influence the electrochemical and dielectric properties, future work and perspectives will be directed toward investigating these characteristics when using larger amounts of Cu dopant.

**Supplementary Materials:** The following supporting information can be downloaded at: <https://www.mdpi.com/article/10.3390/polym14214739/s1>, Figure S1. EDS spectra of 0.5% Cu (CT2), 1% Cu (CT3), 2% Cu (CT4) doped  $\text{TiO}_2$  composites. Figure S2. Elemental mapping images of 2% Cu-

doped TiO<sub>2</sub> (CT4) composite. Figure S3. Histogram plots of average size diameter distribution for pure TiO<sub>2</sub> and 0.5% Cu (CT2), 1% Cu (CT3), 2% Cu (CT4) doped TiO<sub>2</sub> composites.

**Author Contributions:** Conceptualization, P.P.; methodology, P.P.; data curation, P.P., M.H., L.V. and M.A.; formal analysis, P.P., M.H., L.V. and M.A.; investigation, P.P., M.H., L.V. and M.A.; writing—original draft, P.P., M.H. and M.A.; validation, P.P.; writing—review and editing, P.P. and M.H. All authors have read and agreed to the published version of the manuscript.

**Funding:** This research received no external funding.

**Institutional Review Board Statement:** Not applicable.

**Data Availability Statement:** Not applicable.

**Acknowledgments:** This work was supported by a grant from the Ministry of Research, Innovation and Digitization, CNCS—UEFISCDI, project number PN-III-P1-1.1-TE-2021-1068, within PNCDI III.

**Conflicts of Interest:** The authors declare that they have no known competing financial interests or personal relationships that could have appeared to influence the work reported in this paper.

## References

1. Ahirrao, D.J.; Wilson, H.M.; Jha, N. TiO<sub>2</sub>-nanoflowers as flexible electrode for high performance supercapacitor. *Appl. Surf. Sci.* **2019**, *491*, 765–778. [[CrossRef](#)]
2. Da Silva, E.P.; Rubira, A.F.; Ferreira, O.P.; Silva, R.; Muniz, E.C. In situ growth of manganese oxide nanosheets over titanium dioxide nanofibers and their performance as active material for supercapacitor. *J. Colloid Interface Sci.* **2019**, *555*, 373–382. [[CrossRef](#)] [[PubMed](#)]
3. Tian, J.; Zhao, Z.; Kumar, A.; Boughton, R.I.; Liu, H. Recent progress in design, synthesis, and applications of one-dimensional TiO<sub>2</sub> nanostructured surface heterostructures: A review. *Chem. Soc. Rev.* **2014**, *43*, 6920–6937. [[CrossRef](#)] [[PubMed](#)]
4. Abd-Elnaiem, A.M.; Hamdalla, T.A.; Seleim, S.M.; Hanafy, T.A.; Aljohani, M.; Rashad, M. Correction to: Influence of incorporation of gallium oxide nanoparticles on the structural and optical properties of polyvinyl alcohol polymer. *J. Inorg. Org. Polym. Mater.* **2021**, *31*, 4163. [[CrossRef](#)]
5. Ali, N.A.; Abd-Elnaiem, A.M.; Hussein, S.I.; Khalil, A.S.; Alamri, H.R.; Assaedi, H.S. Thermal and Mechanical Properties of Epoxy Resin Functionalized Copper and Graphene Hybrids Using In-situ Polymerization Method. *Curr. Nanosci.* **2021**, *17*, 494–502. [[CrossRef](#)]
6. Khedekar, V.V.; Zaeem, S.M.; Das, S. Graphene-metal oxide nanocomposites for supercapacitors: A perspective review. *Adv. Mater. Lett.* **2018**, *9*, 2–19. [[CrossRef](#)]
7. Afif, A.; Rahman, S.M.H.; Tasfiah Azad, A.; Zaini, J.; Islan, M.A.; Azad, A.K. Advanced materials and technologies for hybrid supercapacitors for energy storage—A review. *J. Energy Storage* **2019**, *25*, 100852. [[CrossRef](#)]
8. Zhang, Z.; Xiao, F.; Guo, Y.; Wang, S.; Liu, Y. One-pot self-assembled three-dimensional TiO<sub>2</sub>-graphene hydrogel with improved adsorption capacities and photocatalytic and electrochemical activities. *ACS Appl. Mater. Interfaces* **2013**, *5*, 2227–2233. [[CrossRef](#)]
9. Heng, I.; Lai, C.W.; Juan, J.C.; Numan, A.; Iqbal, J.; Teo, E.Y.L. Low-temperature synthesis of TiO<sub>2</sub> nanocrystals for high performance electrochemical supercapacitors. *Ceram. Int.* **2019**, *45*, 4990–5000. [[CrossRef](#)]
10. Guan, C.; Xia, X.; Meng, N.; Zeng, Z.; Cao, X.; Soci, C.; Zhang, H.; Fan, H.J. Hollow core-shell nanostructure supercapacitor electrodes: Gap matters. *Energy Environ. Sci.* **2012**, *5*, 59085–59090. [[CrossRef](#)]
11. Dhonde, M.; Sahu, K.; Murty, V.V.S.; Nemala, S.S.; Bhargava, P.; Mallick, S. Enhanced photovoltaic performance of a dye sensitized solar cell with Cu/N Co-doped TiO<sub>2</sub> nanoparticles. *J. Mater. Sci. Mater. Electron.* **2018**, *29*, 6274. [[CrossRef](#)]
12. Wang, H.; Tang, Z.; Sun, L.; He, Y.; Wu, Y.; Li, Z. Capacitance performance enhancement of TiO<sub>2</sub> doped with Ni and graphite. *Rare Met.* **2009**, *28*, 231–236. [[CrossRef](#)]
13. Ning, X.; Wang, X.; Yu, X.; Zhao, J.; Wang, M.; Li, H.; Yang, Y. Outstanding supercapacitive properties of Mn-doped TiO<sub>2</sub> micro/nanostructure porous film prepared by anodization method. *Sci. Rep.* **2016**, *6*, 22634. [[CrossRef](#)]
14. Qian, Y.; Du, J.; Kang, D.J. Enhanced electrochemical performance of porous Co-doped TiO<sub>2</sub> nanomaterials prepared by a solvothermal method. *Microporous Mesoporous Mater.* **2019**, *273*, 148–155. [[CrossRef](#)]
15. Soares, G.B.; Ribeiro, R.A.P.; de Lazaro, S.R.; Ribeiro, C. Photoelectrochemical and theoretical investigation of the photocatalytic activity of TiO<sub>2</sub>:N. *RSC Adv.* **2016**, *6*, 89687–89698. [[CrossRef](#)]
16. Gupta, A.; Sahu, K.; Dhonde, M.; Murty, V.V.S. Novel synergistic combination of Cu/S co-doped TiO<sub>2</sub> nanoparticles incorporated as photoanode in dye sensitized solar cell. *Solar Energy* **2020**, *203*, 296–303. [[CrossRef](#)]
17. Krishnan, S.G.; Archana, P.S.; Vidyadharan, B.; Misonon, I.I.; Vijayan, B.L.; Nair, V.M.; Gupta, A.; Jose, R. Modification of capacitive charge storage of TiO<sub>2</sub> with nickel doping. *J. Alloys Compd.* **2016**, *684*, 328–334. [[CrossRef](#)]
18. Tyagi, A.; Singh, N.; Sharma, Y.; Gupta, R.K. Improved supercapacitive performance in electrospun TiO<sub>2</sub> nanofibers through Ta-doping for electrochemical capacitor applications. *Catal. Today* **2019**, *325*, 33–40. [[CrossRef](#)]

19. Liang, S.; Wang, X.; Qi, R.; Cheng, Y.-J.; Xia, Y.; Müller-Buschbaum, P.; Hu, X. Bronze-phase TiO<sub>2</sub> as anode materials in lithium and sodium-ion batteries. *Adv. Func. Mater.* **2022**, *32*, 2201675. [[CrossRef](#)]
20. Li, X.; Chen, Y.; Zhou, L.; Maia, Y.W.; Huang, H. Exceptional electrochemical performance of porous TiO<sub>2</sub>-carbon nanofibers for lithium ion battery anodes. *J. Mater. Chem. A* **2014**, *2*, 3875–3880. [[CrossRef](#)]
21. Meier, L.A.; Alvarez, A.E.; García, S.G.; del Barrio, M.C. Formation of Cu and Ni nanowires by electrodeposition. *Procedia Mater. Sci.* **2015**, *8*, 617–622. [[CrossRef](#)]
22. Mohamed, M.; Moustafa, S.; Taha, S.A.; Abd-Elnaiem, A.M. Morphological characterization and refractive index calculation of anodized titanium (99.7%) foil in HF-ethanol electrolyte. *Mater. Res. Express* **2018**, *6*, 035026. [[CrossRef](#)]
23. Pascariu, P.; Cojocaru, C.; Samoila, P.; Olaru, N.; Bele, A.; Airinei, A. Novel electrospun membranes based on PVDF fibers embedding lanthanide doped ZnO for adsorption and photocatalytic degradation of dye organic pollutants. *Mater. Res. Bull.* **2021**, *141*, 111376. [[CrossRef](#)]
24. Lal, M.S.; Lavanya, T.; Ramaprabhu, S. An efficient electrode material for high performance solid-state hybrid supercapacitors based on a Cu/CuO/porous carbon nanofiber/TiO<sub>2</sub> hybrid composite. *Beilstein J. Nanotechnol.* **2019**, *10*, 781–793. [[CrossRef](#)]
25. Kumar, M.; Chauhan, H.; Satpati, B.; Deka, S. Yolk type asymmetric Ag-Cu<sub>2</sub>O hybrid nanoparticles on graphene substrate as efficient electrode material for hybrid supercapacitors. *J. Phys. Chem.* **2018**, *233*, 85–104. [[CrossRef](#)]
26. Pascariu, P.; Cojocaru, C.; Samoila, P.; Airinei, A.; Olaru, N.; Rotaru, A.; Romanitan, C.; Tudoran, L.B.; Sucheana, M. Cu/TiO<sub>2</sub> composite nanofibers with improved photocatalytic performance under UV and UV-visible light irradiation. *Surf. Interfaces* **2022**, *28*, 101644. [[CrossRef](#)]
27. Cojocaru, C.; Dorneanu, P.P.; Airinei, A.; Olaru, N.; Samoila, P.; Rotaru, A. Design and evaluation of electrospun polysulfone fibers and polysulfone/NiFe<sub>2</sub>O<sub>4</sub> nanostructured composite as sorbents for oil spill cleanup. *J. Taiwan Inst. Chem. Eng.* **2017**, *70*, 267–281. [[CrossRef](#)]
28. Brunauer, S.; Deming, L.S.; Deming, W.E.; Teller, E. On a theory of the van der Waals adsorption of gases. *J. Am. Chem. Soc.* **1940**, *62*, 1723–1732. [[CrossRef](#)]
29. Pant, B.; Park, M.; Park, S.J. TiO<sub>2</sub> NPs assembled into a carbon nanofiber composite electrode by a one-step electrospinning process for supercapacitor applications. *Polymers* **2019**, *11*, 899. [[CrossRef](#)]
30. Rahimi, N.; Pax, R.A.; Gray, E.; Mac, A. Review of functional titanium oxides. I: TiO<sub>2</sub> and its modifications. *Prog. Solid. State Chem.* **2016**, *44*, 86–105. [[CrossRef](#)]
31. Pascariu, P.; Homocianu, M.; Cojocaru, C.; Samoila, P.; Airinei, A.; Sucheana, M. Preparation of La doped ZnO ceramic nanostructures by electrospinning-calcination method: Effect of La<sup>3+</sup> doping on optical and photocatalytic properties. *Appl. Surf. Sci.* **2019**, *476*, 16–27. [[CrossRef](#)]
32. Türkyilmaz, Ş.Ş.; Güy, N.; Özacar, M. Photocatalytic efficiencies of Ni, Mn, Fe and Ag doped ZnO nanostructures synthesized by hydrothermal method: The synergistic/antagonistic effect between ZnO and metals. *J. Photochem. Photobiol. A Chem.* **2017**, *341*, 39–50. [[CrossRef](#)]
33. Pascariu, P.; Cojocaru, C.; Homocianu, M.; Samoila, P.; Dascalu, A.; Sucheana, M. New La<sup>3+</sup> doped TiO<sub>2</sub> nanofibers for photocatalytic degradation of organic pollutants: Effects of thermal treatment and doping loadings. *Ceram. Int.* **2022**, *48*, 4953–4964. [[CrossRef](#)]
34. Mahmood, P.H.; Amiri, O.; Ahmed, S.S.; Hama, J.R. Simple microwave synthesis of TiO<sub>2</sub>/NiS<sub>2</sub> nanocomposite and TiO<sub>2</sub>/NiS<sub>2</sub>/Cu nanocomposite as an efficient visible driven photocatalyst. *Ceram. Int.* **2019**, *45*, 14167–14172. [[CrossRef](#)]
35. Ganesh, I.; Kumar, P.P.; Annapoorna, I.; Sumliner, J.M.; Ramakrishna, M.; Hebalkar, N.Y.; Padmanabham, G.; Sundararajan, G. Preparation and characterization of Cu-doped TiO<sub>2</sub> materials for electrochemical, photoelectrochemical, and photocatalytic applications. *Appl. Surf. Sci.* **2014**, *293*, 229–247. [[CrossRef](#)]
36. Cheng, J.P.; Fang, J.H.; Li, M.; Zhang, W.F.; Liu, F.; Zhang, X.B. Enhanced electrochemical performance of CoAl-layered double hydroxide nanosheet arrays coated by platinum films. *Electrochim. Acta* **2013**, *114*, 68–75. [[CrossRef](#)]
37. Poudel, M.B.; Yu, C.; Kim, H.J. Synthesis of conducting bifunctional polyaniline@Mn-TiO<sub>2</sub> nanocomposites for supercapacitor electrode and visible light driven photocatalysis. *Catalysts* **2020**, *10*, 546. [[CrossRef](#)]
38. Pan, C.; Sun, H.; Gao, J.; Hu, Y.; Wang, J. Simplified synthesis of 3D flexible reduced graphene oxide-wrapped NiCo<sub>2</sub>O<sub>4</sub> nanowires for high-performance supercapacitor. *Nanosci. Nanotechnol. Lett.* **2018**, *10*, 358–364. [[CrossRef](#)]
39. Cao, X.; Shi, Y.; Shi, W.; Lu, G.; Huang, X.; Yan, Q.; Zhang, Q.; Zhang, H. Preparation of novel 3D graphene networks for supercapacitor applications. *Small* **2011**, *7*, 3163–3168. [[CrossRef](#)]
40. Li, P.; Ruan, C.; Xu, J.; Xie, Y. A high-performance asymmetric supercapacitor electrode based on a three-dimensional ZnMoO<sub>4</sub>/CoO nanohybrid on nickel foam. *Nanoscale* **2019**, *11*, 13639–13649. [[CrossRef](#)]
41. Wang, Q.; Wang, J.; Wang, H.; Zhan, J.; Zhu, Y.; Zhang, Q.; Shen, Q.; Yang, H. TiO<sub>2</sub>-C nanowire arrays@polyaniline core-shell nanostructures on carbon cloth for high performance supercapacitors. *Appl. Surf. Sci.* **2019**, *493*, 1125–1133. [[CrossRef](#)]
42. Haque, M.; Li, Q.; Kuzmenko, V.; Smith, A.D.; Enoksson, P. Ionic liquid electrolyte for supercapacitor with high temperature compatibility. *J. Phys. Conf. Ser.* **2017**, *922*, 012011. [[CrossRef](#)]
43. He, X.; Yang, C.P.; Zhang, G.L.; Shi, D.W.; Huang, Q.A.; Xiao, H.B.; Liu, Y.; Xiong, R. Supercapacitor of TiO<sub>2</sub> nanofibers by electrospinning and KOH treatment. *Mater. Des.* **2016**, *106*, 74–80. [[CrossRef](#)]
44. Li, H.; Wu, D.; Zhu, X.; Yang, C.; Liu, D.; Chen, X.; Song, Y.; Lu, L. High-performance and renewable supercapacitors based on TiO<sub>2</sub> nanotube array electrodes treated by an electrochemical doping approach. *Electrochim. Acta* **2014**, *116*, 129–136. [[CrossRef](#)]

45. Vidyadharan, B.; Archana, P.S.; Ismail, J.; Yusoff, M.M.; Jose, R. Improved supercapacitive charge storage in electrospun niobium doped titania nanowires. *RSC Adv.* **2015**, *5*, 50087–50097. [[CrossRef](#)]
46. Samet, M.; Levchenko, V.; Boiteux, G.; Seytre, G.; Kallel, A.; Serghei, A. Electrode polarization vs. Maxwell-Wagner-Sillars interfacial polarization in dielectric spectra of materials: Characteristic frequencies, and scaling laws. *J. Chem. Phys.* **2015**, *142*, 194703. [[CrossRef](#)]
47. Asandulesa, M.; Kostromin, S.; Aleksandrov, A.; Tameev, A.; Bronnikov, S. The effect of PbS quantum dots on molecular dynamics and conductivity of PTB7:PC71BM bulk heterojunction as revealed by dielectric spectroscopy. *Phys. Chem. Chem. Phys.* **2022**, *24*, 9589–9596. [[CrossRef](#)]
48. Pochard, I.; Vall, M.; Eriksson, J.; Farineau, C.; Cheung, O.; Frykstrand, S.; Welch, K.; Stromme, M. Amine-functionalised mesoporous magnesium carbonate: Dielectric spectroscopy studies of interactions with water and stability. *Mater. Chem. Phys.* **2018**, *216*, 332–338. [[CrossRef](#)]
49. Asandulesa, M.; Kostromin, S.; Tameev, A.; Aleksandrov, A.; Bronnikov, S. Molecular dynamics and conductivity of a PTB7:PC71BM photovoltaic polymer blend: A dielectric spectroscopy study. *ACS Appl. Polym. Mater.* **2021**, *3*, 4869–4878. [[CrossRef](#)]
50. Larsson, O.; Said, E.; Berggren, M.; Crispin, X. Insulator polarization mechanisms in polyelectrolyte-gated organic field-effect transistors. *Adv. Funct. Mater.* **2009**, *19*, 3334–3341. [[CrossRef](#)]